

IEEE TRANSACTIONS ON GEOSCIENCE AND REMOTE SENSING

A PUBLICATION OF THE IEEE GEOSCIENCE AND REMOTE SENSING SOCIETY



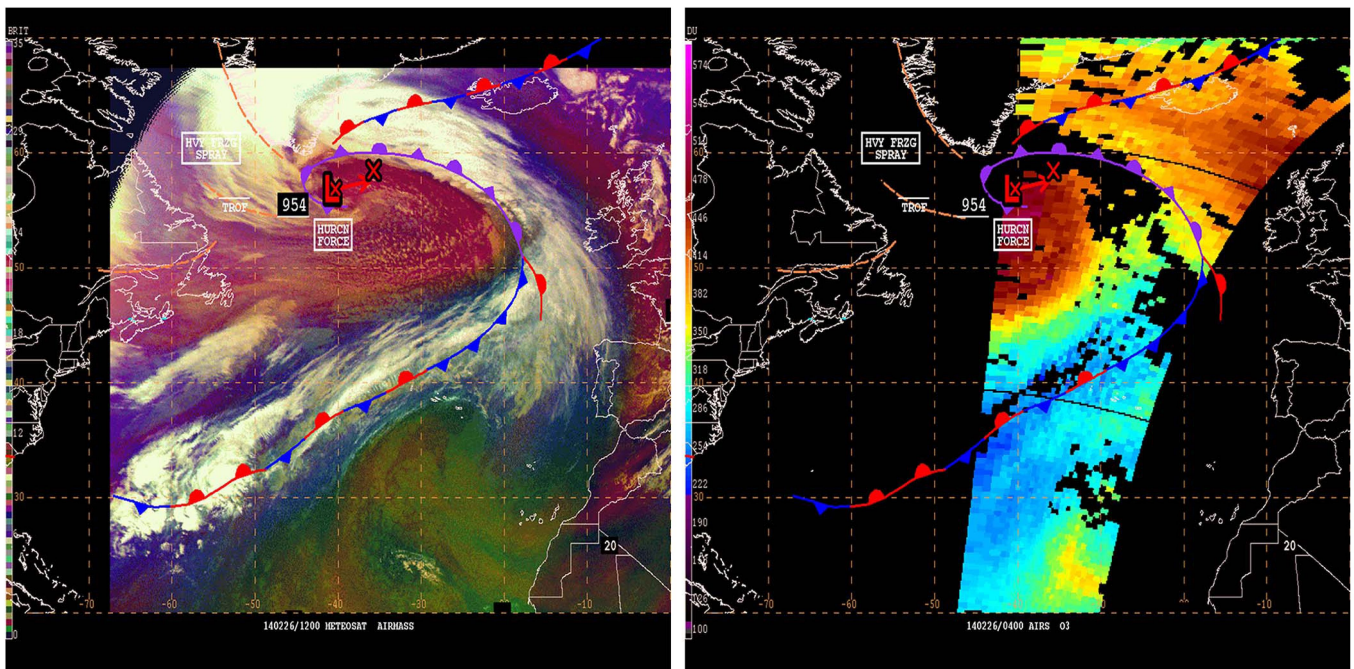
FEBRUARY 2016

VOLUME 54

NUMBER 2

IGRSD2

(ISSN 0196-2892)



Satellite perspective of a rapidly intensifying North Atlantic extratropical cyclone. NOAA Ocean Prediction Center surface analysis overlaid on Meteosat Spinning Enhanced Visible and Infrared Imager RGB Air Mass imagery (left) and Atmospheric Infrared Sounder total column ozone (right).

IEEE TRANSACTIONS ON GEOSCIENCE AND REMOTE SENSING

A PUBLICATION OF THE IEEE GEOSCIENCE AND REMOTE SENSING SOCIETY



FEBRUARY 2016

VOLUME 54

NUMBER 2

IGRSD2

(ISSN 0196-2892)

PAPERS

Atmosphere

- A Comprehensive Evaluation and Analysis of the Performance of Multiple Tropospheric Models in China Region. *B. Chen and Z. Liu* 663
- Bridging InSAR and GPS Tomography: A New Differential Geometrical Constraint *P. Benevides, G. Nico, J. Catalão, and P. M. A. Miranda* 697
- Analysis of Desert Dust Outbreaks Over Southern Europe Using CALIOP Data and Ground-Based Measurements. *C. R. Marcos, R. Pedrós, J. L. Gómez-Amo, M. P. Utrillas, and J. A. Martínez-Lozano* 744
- Development and Application of Atmospheric Infrared Sounder Ozone Retrieval Products for Operational Meteorology *E. B. Berndt, B. T. Zavadsky, and M. J. Folmer* 958
- Comparison of Typhoon Centers From SAR and IR Images and Those From Best Track Data Sets *G. Zheng, J. Yang, A. K. Liu, X. Li, W. G. Pichel, and S. He* 1000

Oceans

- Estimation of the Ocean Water Albedo From Remote Sensing and Meteorological Reanalysis Data *Y. Feng, Q. Liu, Y. Qu, and S. Liang* 850
- Ocean Vector Winds From WindSat Two-Look Polarimetric Radiances *K. A. Hilburn, T. Meissner, F. J. Wentz, and S. T. Brown* 918
- Generalized Linear Observables for Ocean Wind Retrieval From Calibrated GNSS-R Delay-Doppler Maps. *N. Rodriguez-Alvarez and J. L. Garrison* 1142

Vegetation and Land

- Improved Salient Feature-Based Approach for Automatically Separating Photosynthetic and Nonphotosynthetic Components Within Terrestrial Lidar Point Cloud Data of Forest Canopies *L. Ma, G. Zheng, J. U. H. Eitel, L. M. Moskal, W. He, and H. Huang* 679
- Evaluating NDVI Data Continuity Between SPOT-VEGETATION and PROBA-V Missions for Operational Yield Forecasting in North African Countries *M. Meroni, D. Fasbender, R. Balaghi, M. Dali, M. Haffani, I. Haythem, J. Hooker, M. Lahlou, R. Lopez-Lozano, H. Mahyou, M. Ben Moussa, N. Sghaier, T. Wafa, and O. Leo* 795
- Estimating the Hemispherical Broadband Longwave Emissivity of Global Vegetated Surfaces Using a Radiative Transfer Model. *J. Cheng, S. Liang, W. Verhoef, L. Shi, and Q. Liu* 905
- Estimation of Vegetation Water Content From the Radar Vegetation Index at L-Band *Y. Huang, J. P. Walker, Y. Gao, X. Wu, and A. Monerris* 981

(Contents Continued on Page 630)



Subsurface and Geology	
Synchrosqueezing S-Transform and Its Application in Seismic Spectral Decomposition	817
Feasibility and Limitations of Void Detection Using Gravity Gradiometry	881
Electromagnetics	
Copolarized and Cross-Polarized Backscattering From Random Rough Soil Surfaces From L-Band to Ku-Band Using Numerical Solutions of Maxwell's Equations With Near-Field Precondition	651
A Meshless Method of Solving Inverse Scattering Problems for Imaging Dielectric Objects	990
Transient Electromagnetic Scattering of a Metallic Object Buried in Underwater Sediments	1091
Hyperspectral Data Processing	
Matrix-Based Discriminant Subspace Ensemble for Hyperspectral Image Spatial-Spectral Feature Fusion	783
Integrating Hierarchical Segmentation Maps With MRF Prior for Classification of Hyperspectral Images in a Bayesian Framework	805
Intrinsic Representation of Hyperspectral Imagery for Unsupervised Feature Extraction	1118
Multiclass Object Detection With Single Query in Hyperspectral Imagery Using Class-Associative Spectral Fringe-Adjusted Joint Transform Correlation	1196
Image Processing and Analysis	
Improving the Consistency of Multitemporal Land Cover Maps Using a Hidden Markov Model	703
Hashing-Based Scalable Remote Sensing Image Search and Retrieval in Large Archives	892
Geo-Information Systems	
DEM-Assisted RFM Block Adjustment of Pushbroom Nadir Viewing HRS Imagery	1025
Microwave Radiometry	
GCOM-W1 AMSR2 Level 1R Product: Dataset of Brightness Temperature Modified Using the Antenna Pattern Matching Technique	770
Boreal, Temperate, and Tropical Forests as Vicarious Calibration Sites for Spaceborne Microwave Radiometry	1035
Calibration to Improve Forward Model Simulation of Microwave Emissivity at GPM Frequencies Over the U.S. Southern Great Plains	1103
Radar Systems	
Uncertainty Estimates in the SMAP Combined Active-Passive Downscaled Brightness Temperature	640
Radar Attenuation and Reflectivity Measurements of Snow With Dual Ka-Band Radar	714
Unified Huynen Phenomenological Decomposition of Radar Targets and Its Classification Applications	723
Bistatic Radar Measurements of Significant Wave Height Using Signals of Opportunity in L-, S-, and Ku-Bands	826
Space-Time Adaptive Processing and Motion Parameter Estimation in Multistatic Passive Radar Using Sparse Bayesian Learning	944
Experimental Characterization of Polarimetric Radar Backscatter Response of Distributed Targets at High Millimeter-Wave Frequencies	1013
A Novel High-Precision Phase-Derived-Range Method for Direct Sampling LFM Radar	1131

Synthetic Aperture Radar	
First Bistatic Demonstration of Digital Beamforming in Elevation With TerraSAR-X as an Illuminator	842
. <i>R. Wang, W. Wang, Y. Shao, F. Hong, P. Wang, Y. Deng, Z. Zhang, and O. Loffeld</i>	
The Influence of Equatorial Scintillation on L-Band SAR Image Quality and Phase	869
. <i>F. J. Meyer, K. Chotoo, S. D. Chotoo, B. D. Huxtable, and C. S. Carrano</i>	
Classification of Polarimetric SAR Images Based on Modeling Contextual Information and Using Texture Features.	932
. <i>A. Masjedi, M. J. Valadan Zoej, and Y. Maghsoudi</i>	
Robust Estimators for Multipass SAR Interferometry.	968
. <i>Y. Wang and X. X. Zhu</i>	
High-Resolution SAR-Based Ground Moving Target Imaging With Defocused ROI Data	1062
. <i>Y. Zhang, J. Sun, P. Lei, G. Li, and W. Hong</i>	
A Phase-Decomposition-Based PSInSAR Processing Method.	1074
. <i>N. Cao, H. Lee, and H. C. Jung</i>	
Terrain and Surface Modeling Using Polarimetric SAR Data Features	1170
. <i>R. Sabry</i>	
Improved InSAR Phase Noise Filter in Frequency Domain	1185
. <i>Z. Suo, J. Zhang, M. Li, Q. Zhang, and C. Fang</i>	
Improved DBF Algorithm for Multichannel High-Resolution Wide-Swath SAR	1209
. <i>B. Liu and Y. He</i>	
Lidar Systems	
A Wavelet-Based Echo Detector for Waveform LiDAR Data.	757
. <i>C.-K. Wang, Y.-H. Tseng, and C.-K. Wang</i>	
Object Classification and Recognition From Mobile Laser Scanning Point Clouds in a Road Environment.	1226
. <i>M. Lehtomäki, A. Jaakkola, J. Hyypä, J. Lampinen, H. Kaartinen, A. Kukko, E. Puttonen, and H. Hyypä</i>	
Satellite Systems	
Suomi-NPP VIIRS Solar Diffuser Stability Monitor Performance.	631
. <i>J. Fulbright, N. Lei, B. Efremova, and X. Xiong</i>	
Lunar Calibration and Performance for S-NPP VIIRS Reflective Solar Bands	1052
. <i>X. Xiong, J. Sun, J. Fulbright, Z. Wang, and J. J. Butler</i>	
Local Adaptive Calibration of the Satellite-Derived Surface Incident Shortwave Radiation Product Using Smoothing Spline.	1156
. <i>X. Zhang, S. Liang, Z. Song, H. Niu, G. Wang, W. Tang, Z. Chen, and B. Jiang</i>	

CORRESPONDENCE	
Comment on “Measurement of Ionospheric TEC in Spaceborne SAR Data”	1240
. <i>Y. Zhang, M. Jehle, L. Li, Z. Dong, and D. Liang</i>	

About the Cover: The cover shows a satellite perspective of a rapidly intensifying North Atlantic extratropical cyclone on 26 February 2014. Comparison of 1200 UTC Meteosat Spinning Enhanced Visible and Infrared Imager (SEVIRI) RGB Air Mass imagery (left) and 0400 UTC Atmospheric Infrared Sounder (AIRS) total column ozone in Dobson Units (Right). The Ocean Prediction Center surface analysis valid at 1200 UTC is overlaid on each image to show the location of the surface low pressure and region of anticipated hurricane-force winds. The RGB Air Mass imagery has been used by the Ocean Prediction Center to identify regions of stratospheric air (red/orange coloring south of the low-pressure center), which play a key role in rapid cyclogenesis and hurricane-force wind events. Due to the qualitative nature of the RGB Air Mass imagery, the NASA Short-term Prediction, Research, and Transition Center (SPoRT) worked closely with the Geostationary Operational Environmental Satellite-R (GOES-R) series and Joint Polar Satellite System (JPSS) Proving Grounds to develop ozone products derived from AIRS to enhance forecaster interpretation and confidence in the RGB Air Mass imagery during rapid cyclogenesis and high-wind events. Higher ozone values detected by AIRS correlate closely with the red/orange region on the RGB Air Mass image to indicate stratospheric air influence on the extratropical cyclone. For more information please see “Development and Application of Atmospheric Infrared Sounder Ozone Products for Operational Meteorology,” by Berndt *et al.*, which begins on page 958.